Supplementary Information for

"A machine-learned interatomic potential for silica and its relation to empirical models"

Linus C. Erhard,[1] Jochen Rohrer,[1,*] Karsten Albe,[1,†] and Volker L. Deringer[2,‡]

[1]*Institute of Materials Science, Technische Universität Darmstadt,*
Otto-Berndt-Strasse 3, D-64287 Darmstadt, Germany
[2]*Department of Chemistry, Inorganic Chemistry Laboratory,*
University of Oxford, Oxford OX1 3QR, United Kingdom

SUPPLEMENTARY METHODS

We used an iterative procedure to train the Gaussian approximation potential (GAP) based on density functional theory (DFT) calculated energies and forces, gradually improving the composition of the reference ('training') database and accordingly the performance of the potential. In each iteration, the training database consisted of structural models ('structures' in the following) describing various crystalline silica phases, dimer and small cluster structures in supercells, as well as amorphous and liquid model systems. Although the database contains a small number of crystalline structures for elemental silicon, we would like to emphasise that the potential is created to describe only the stoichiometric SiO_2 system accurately.

For structural models describing crystalline phases, strains were applied and the atomic positions were randomly displaced using the `rattle()` functionality of the Atomic Simulation Environment (ASE).[1] These training structures were kept fixed in each iteration. Amorphous and liquid structures were extracted from molecular dynamics (MD) simulations and added during every iteration. After every iteration cycle, the latest version of the GAP was used for MD simulations, such as melt–quenching runs to generate new training structures.

In total (after the last iteration) the database contains 3074 structures, of which 2000 are crystalline structures, 939 are amorphous or liquid structures, and 135 are dimer and cluster structures. In the following, we describe the procedures and parameters used for preparing individual training structures.

A. Density functional theory calculations and molecular-dynamics simulations

DFT calculations were performed using the GPAW[2,3] and VASP[4–7] codes employing the projector augmented wave method.[8,9] Supplementary Figure 1 shows the energy differences between different silica polymorphs calculated using the LDA,[10–12] PBE,[13] PBEsol,[14] and SCAN[15] functionals. These energy differences are compared with differences in the experimental enthalpies of formation at room temperature. Both, PBEsol and SCAN perform considerably better than LDA and PBE; the latter two fail to describe silica accurately. As already investigated earlier, PBE gives accurate energy barriers to high-pressure polymorphs

like stishovite and coesite, while it fails for low-pressure polymorphs like α-cristobalite and tridymite.[16] In contrast, LDA shows accurate behaviour for low-pressure polymorphs and fails for high-pressure polymorphs. For example, it predicts stishovite to be more stable than α-quartz. Only PBEsol and SCAN predict α-quartz to be the most stable phase at 0 K and zero pressure. However, PBEsol underestimates the energy difference to stishovite significantly. Overall, SCAN shows very good agreement with the experimental energy differences, or at least as for moganite slightly better agreement than the other functionals. LDA, PBE, and PBEsol calculations were performed using GPAW using an energy cutoff of 700 eV and a k-spacing of 0.279 Å^{-1}; SCAN calculations were performed using VASP with an energy cutoff of 900 eV and a k-spacing of 0.23 Å^{-1}. We initially used PBEsol to compute energies and forces for our database. To improve the accuracy of the GAP, we eventually re-calculated the values in the database using the computationally more demanding SCAN functional.

MD simulations were performed using LAMMPS,[17] a Nosé–Hoover thermostat[18,19] for NVT and additionally a Parrinello–Rahman barostat[20] for NPT simulations. We used a time step of 1 fs, a temperature damping constant of 100 fs and a pressure damping constant of 1000 fs.

B.   Training structures

1.   Dimers and clusters

We used data describing the energy and forces as a function of the bond length for isolated Si–Si, O–O and Si–O dimers. In these, the bond lengths were varied from 5 Å with increments of 0.05 Å to lower bond distances. All dimers with absolute force below 40 eV/Å were added to the database. Moreover, to avoid the formation of oxygen agglomerates in amorphous models, small oxygen clusters consisting of up to 5 atoms were added to the database. These clusters appeared in melt–quench simulations during early iterations and were extracted from there. To avoid too large forces the structures were scaled with factors of 1.5, 2.0, 2.5 and 3.0. As reference structures isolated silicon and oxygen atoms in cells with lengths of 20 Å in each direction were added to the database.

2. Crystalline phases

The following crystalline phases were part of the training structures: α-quartz, coesite, stishovite, chabazite, moganite, α-cristobalite, low temperature tridymite, β-cristobalite, β-quartz, β-tridymite and tridymite in the $C222_1$ and the $P2_12_12_1$ modification. Reference structures for each phase were retrieved from the Inorganic Crystal Structure Database (ICSD).[21] For each reference structure, we then generated 30 isotropically deformed training structures with strains between $\pm5\%$ and 70 randomly strained structures with diagonal strains between $\pm2.5\%$ and angular strains between $\pm5\%$. In each of these training structures, additional random displacements were applied to the atomic positions using the `ase.rattle()`[1] function with a standard deviation of 0.01 Å. For the low-temperature polymorphs we further generated 100 training structures by randomly straining ($\pm2.5\%$ for diagonal and $\pm5\%$ for angular strains) structures taken from the hydrostatic energy–volume curve. The same procedure was used for silicon structures in the diamond modification to improve the description of the many-body Si–Si interaction.

3. Amorphous structures

Amorphous structures were prepared by melt–quench simulations using MD simulations. The details of the individual procedure depend on the iteration step, see Table I. As starting configuration we used either β-cristobalite or a random distribution of atoms with a mass density between 2 and 3 g/cm^3 (experimental density ≈ 2.2 g/cm^3).[22] β-cristobalite has the advantage that its conventional unit cell is cubic, such that the construction of an initial supercell is straightforward. We use either NVT simulations (to keep the density constant) or NPT simulations. In each iteration, we performed 100 MD simulations in parallel with varying pressures for NPT simulations and varying densities for NVT simulations. From each simulation, we extracted three snapshots: one after equilibrating the liquid, one in the middle of the quenching process, and one after the equilibration of the amorphous phase. The simulations were performed as follows:

1. Random initialisation of atomic positions and randomization for 10 ps at 6000 K under NVT conditions or starting from a β-cristobalite supercell

2. Equilibration of the liquid for 10 ps (NVT or NPT)

4

3. Quenching to room temperature (NVT or NPT)

4. Equilibration for 10 ps at 300 K (NVT or NPT)

The temperature of the liquid phase was set depending on the density or applied pressure. For pressures of 0 GPa and densities of 2 g/cm^3 the temperature was set to 3000 K; for pressures of 10 GPa and densities of 3 g/cm^3 the temperature was set to 4000 K. Between these regions, the temperature was scaled linearly. In the NPT simulations, the pressure was logarithmically scaled between 1 GPa and 10 GPa. In the last iteration, we performed only 20 simulations in parallel. In addition, we removed the structures initially generated with the Broughton potential from the database to make the potential more uniform. In order to avoid overfitting due to large forces, only structures with maximum DFT forces below 40 eV/Å were added to the database. We would to emphasise that we also tested including data from further iterations. However, we observed that adding more amorphous and liquid data decreased the accuracy for crystalline phases, while it did not markedly improve the description of the amorphous phases.

C. GAP model fitting

Supplementary Table II shows the key parameters used for the GAP fit. For a detailed description of these parameters, we refer to ref. 23. In addition to these parameters, we emphasise that the fitting approach uses regularisation. The regularisation is important to ensure a stable fit, and helps to account for the fact that the DFT energies and forces contain an uncertainty. Regularisation allows for deviations from the target values by reducing the penalisation when the deviations are in a certain range. This reduces the tendency to overfit energies and forces of, in particular, less favourable structures. For amorphous and cluster structures we use regularisation values ('expected errors'; see ref. 24 for a discussion of this point) of 0.01 eV/atom for the energies and 0.3 eV/Å for the forces; for crystalline structures, we use 0.005 eV/atom for the energy and 0.05 eV/Å for the forces. As energy reference, we use the isolated silicon and oxygen atoms.

D.   Tests for crystalline phases

For studying the transition of stishovite to $CaCl_2$-type silica, we started from $8 \times 8 \times 10$ supercell expansions of the (rutile-type) stishovite unit cell. Theses supercells were equilibrated for 10 ps at 300 K and a given pressure between 50 GPa and 90 GPa. Subsequently the lattice parameters were determined for another 10 ps.

E.   Tests for liquid and amorphous phases

Diffusion coefficients were determined using mean square displacements and the Einstein relation as done by Carré *et al.* (ref. 25). As input, we used liquid structures generated by the GAP using the quenching procedure described above, however, with a target temperature of 2373 K. This structure was annealed in 40 ps to different temperatures (3000 K, 3250 K, 3500 K, 3750 K or 4000 K) and equilibrated at this temperature for 10 ps. For the next 200 ps the temperature was kept constant and the mean square displacements were determined. The energy barriers were obtained by an Arrhenius fit to the self-diffusion constants.
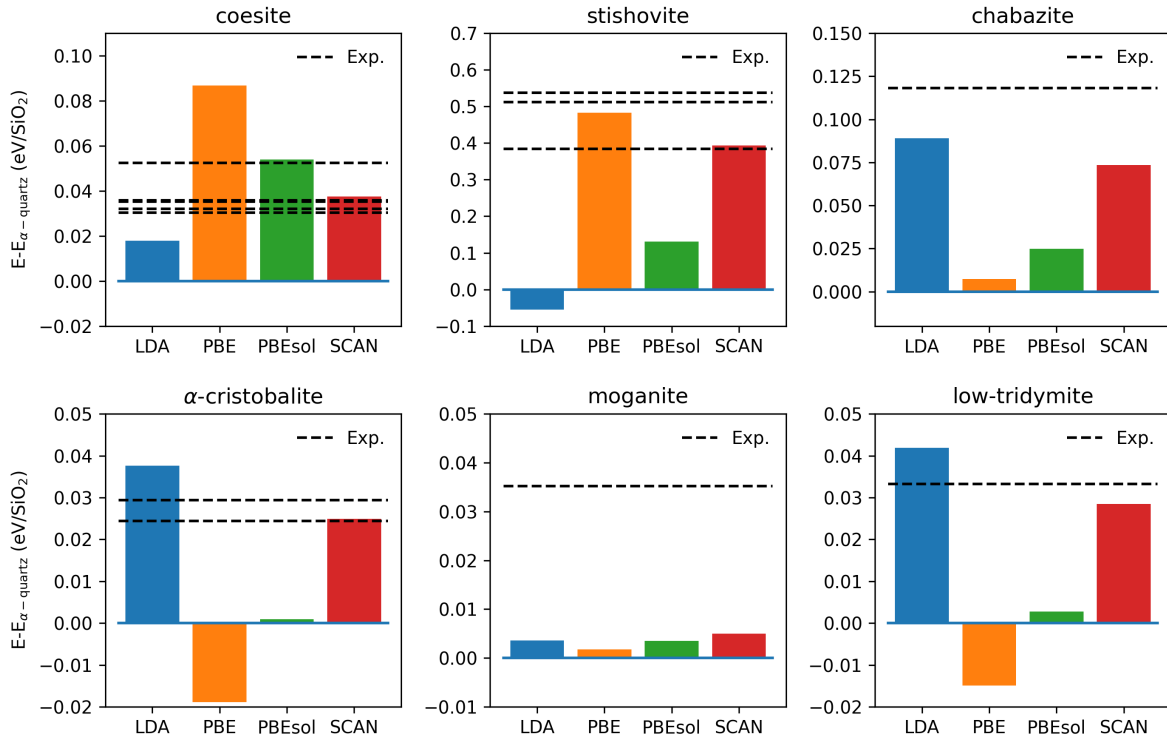
Supplementary Figure 1. Energetic hierarchy of various silica phases in eV/f.u. ($E - E_0$, where E is the total energy per formula unit and E_0 correspond to the energy of α-quartz). Experimental values correspond to differences in standard enthalpies of formation at room temperature. Positive (negative) values indicate that a phase is less stable (more stable) than α-quartz. Experimental data are taken from Refs. 26–30 for coesite, Refs. 26, 28, and 30 for stishovite, Ref. 31 for chabazite, Refs. 32 and 33 for α-cristobalite, Ref. 34 for moganite and Ref. 32 for low temperature tridymite.

Supplementary Table I. Details of the melt-quench simulations to prepare amorphous models.

Iteration	Potential	Start	Randomization	Ensemble	Structures	Quench rate (Ks^{-1})
1	Broughton	Random	True	NVT/NPT	300	10^{10}–10^{12}
2	GAP	β-cristobalite	False	NVT	150	10^{15}
3	GAP	β-cristobalite	False	NVT	129	10^{15}
4	GAP	β-cristobalite	False	NVT	300	10^{15}
Add oxygen clusters						
5	GAP	Random	True	NVT	300	10^{15}
Remove structures from first iteration						
Recalculate database with SCAN						
6	GAP	Random	True	NVT	60	10^{13}

Supplementary Table II. Parameters used for GAP fitting. For a detailed description of individual parameters, see Ref. 23.

	2-body			SOAP
	O–O	Si–Si	Si–O	
δ (eV)	4.0	4.0	4.0	0.4
Θ	1.25	2.0	2.0	
r_{cut} (Å)	5.0	5.0	5.0	5.0
r_Δ (Å)				1.0
σ_{at} (Å)				0.5
n_{max}				12
l_{max}				4
ζ				4
Sparsification		Uniform		CUR
N_{sparse}(amorphous)				1000
N_{sparse}(mid-quench)				1000
N_{sparse}(liquid)				1000
N_{sparse}(crystalline)				1000
N_{sparse}(cluster)				60
N_{sparse}(total)	15	15	15	4060

Supplementary Table III. Details of the calculations for the quality estimates in Fig. 7.

| Property	Calculation
FSDP height	if $H_{\exp_1}^{\max} < H_{\text{Potential}}^{\max} < H_{\exp_2}^{\max} \to 1$ else $\to 1 - (H_{\text{Potential}}^{\max} - H_{\exp_1}^{\max})/(H_{\exp_1}^{\max} - H_{12}^{\min})$
$\Delta S(q)$	$1 - \text{MIN}\left(\int_{0.5 \mathring{A}^{-1}}^{17.7 \mathring{A}^{-1}} \left\| S_{\text{Potential}}(k) - S_{\text{Exp}_1}(k) \right\| dk, \int_{0.5 \mathring{A}^{-1}}^{17.7 \mathring{A}^{-1}} \left\| S_{\text{Potential}}(k) - S_{\text{Exp}_2}(k) \right\| dk \right)/A_{\text{ref}}$ $A_{\text{ref}} = \left(\int_{0.5 \mathring{A}^{-1}}^{17.7 \mathring{A}^{-1}} S_{\text{Exp}_1}(k) dk + \int_{0.5 \mathring{A}^{-1}}^{17.7 \mathring{A}^{-1}} S_{\text{Exp}_2}(k) dk \right)/10$
Coordination (amorphous)	$\dfrac{2 - \log_{10}(\text{Total defects}/\%)}{3}$
$\Delta H(\text{a–c})$	$1 - \dfrac{\Delta E_{\text{Potential}} - 131 \text{ meV}}{2000 \text{ meV}}$
Elastic constants	$1 - \left(\dfrac{\text{MAPE}_{\text{Potential}}^{\text{ELASTIC}}}{300\%} \right) \dfrac{N_{\text{Des.-Polymorphs}}}{N_{\text{Tot.-Polymorphs}}}$
Lattice parameters	$\left(1 - \dfrac{\text{MAPE}_{\text{Potential}}^{\text{LATTICE}}}{5\%} \right) \dfrac{N_{\text{Des.-Polymorphs}}}{N_{\text{Tot.-Polymorphs}}}$
Phase diagram	$\text{Coesite}_{\text{Transition}} + \text{Stishovite}_{\text{Transition}}$ $\text{Coesite}_{\text{Transition}} = 0.5 - \text{MIN}\left(\left(\sum_{T \in (600,700,800)} \left\| P_{\exp}^{\text{coesite}}(T) - P_{\text{Potential}}^{\text{coesite}}(T) \right\| \right)/12, 0.5 \right)$ $\text{Stishovite}_{\text{Transition}} = 0.5 - \text{MIN}\left(\left(\sum_{T \in (800,900,1000)} \left\| P_{\exp}^{\text{stishovite}}(T) - P_{\text{Potential}}^{\text{stishovite}}(T) \right\| \right)/12, 0.5 \right)$
Speed	$\dfrac{3 - \log_{10}(\text{runtime}/s)}{5}$

H^{max}	Height of the first sharp diffraction peak of the experimental structure factor data[35,36] and the potential.
H^{min}_{12}	Height of the minimum between first peak and second peak (average of experimental structure factor data).
$S(k)$	Structure factor data from experiment or from amorphous structures generated by potentials.
Total defects	Proportion of not perfectly coordinated atoms in amorphous structures.
$\Delta E_{\mathrm{Potential}}$	GAP energy difference between relaxed amorphous structure and α-quartz in eV/SiO$_2$.
$\mathrm{MAPE}^{\mathrm{ELASTIC}}_{\mathrm{Potential}}$	Mean absolute percentage error of elastic constants predicted by a potential compared to experiment.[37–40]
$\mathrm{MAPE}^{\mathrm{LATTICE}}_{\mathrm{Potential}}$	Mean absolute percentage error of lattice parameters predicted by a potential compared to experiment.[41–47]
$N_{\mathrm{Tot.\text{-}Polymorphs}}$	Number of polymorphs for which experimental data is available.
$N_{\mathrm{Des.\text{-}Polymorphs}}$	Number of polymorphs for which experimental data is available and which are described by the potential.
$P^{\mathrm{coesite}}(T)$	Transition pressure between α-quartz and coesite predicted by the potential or experiment[48] at temperature T.
$P^{\mathrm{stishovite}}(T)$	Transition pressure between coesite and stishovite predicted by the potential or experiment[28] at temperature T.
runtime	Time for molecular dynamics simulation running on 1 core over 100 time steps with 64 formula units.

Supplementary Table IV. Values of the quality estimates in Fig. 7, calculated by the formulas in Supp. Tab. III.

| $\times 10^{-1}$	GAP	CHIK	BKS	Munetoh	Vashishta	Broughton
FSDP (height)	6.2	8.8	9.9	5.3	8.5	—
$\Delta S(q)$	7.4	7.8	5.9	5.8	6.6	—
Coordination (amorphous)	9.4	7.0	6.3	3.2	6.1	—
$\Delta H(a-c)$	9.0	9.1	8.8	4.7	8.8	—
Elastic constants	8.9	8.9	8.8	6.0	2.3	5.7
Lattice parameters	9.1	6.6	7.2	3.6	3.4	6.4
Phase diagram	8.5	0.9	0	6.4	0	3.2
Speed	1.7	7.5	6.7	9.2	7.3	8.5
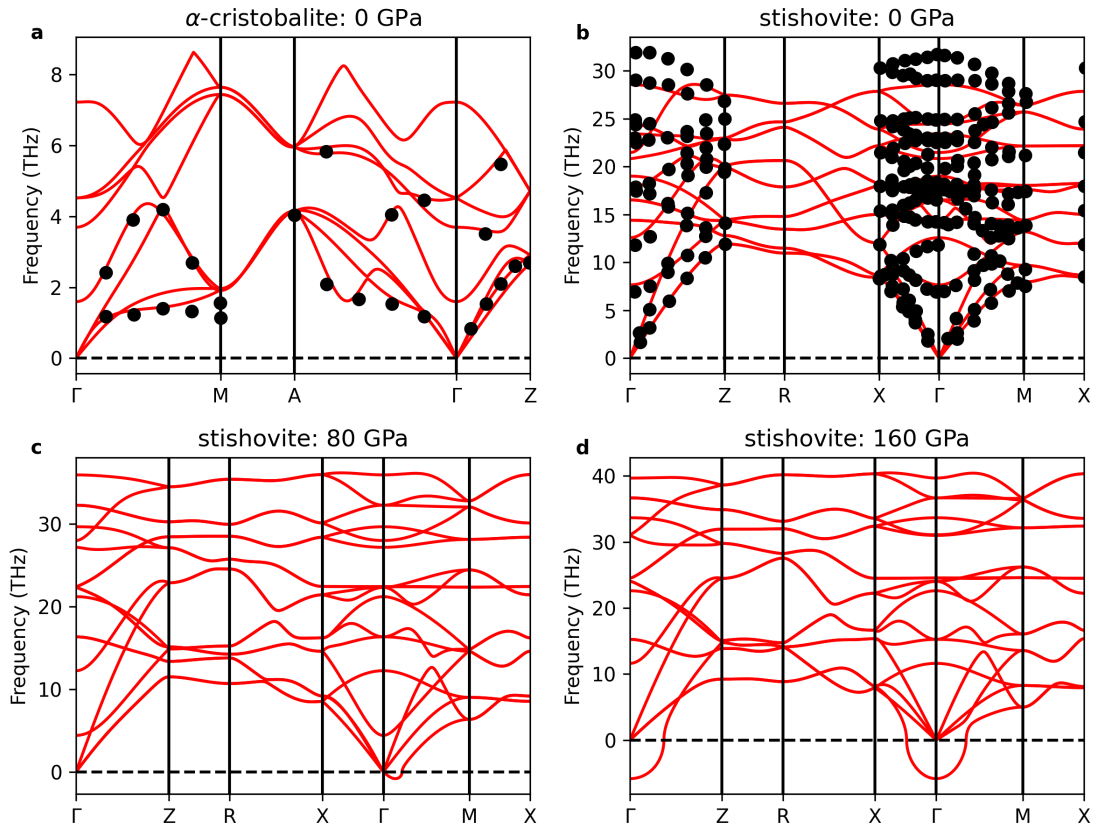
Supplementary Figure 2. Phonon dispersion curves for (a) α-cristobalite at 0 GPa, (b) stishovite at 0 GPa, (c) stishovite at 80 GPa, (d) stishovite at 160 GPa. The red curves are calculated by GAP using the quasi-harmnic approximation, while the black dots are experimental results from Wehinger *et al.* for α-cristobalite and Bosak *et al.* for stishovite.[49,50]
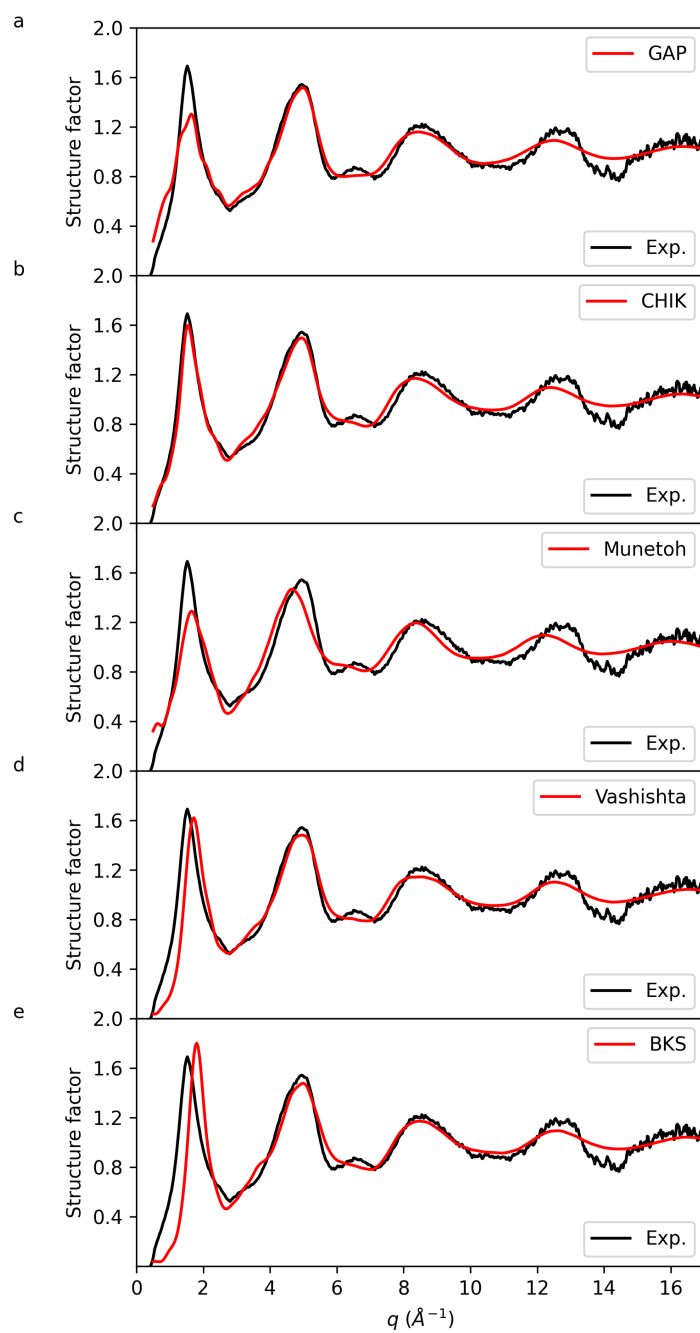
Supplementary Figure 3. Structure factors of liquid structures generated using (a) the GAP, (b) the CHIK, (c) the Munetoh, (d) the Vashishta and (e) the BKS potential. The experimental values are from Mei *et al.*[36] The structures are generated in the same way as the amorphous structures, despite, the final target temperature was set to 2100 °C.

Supplementary Table V. Excess energies of large-scale models generated by combined CHIK and GAP molecular dynamics simulations. A CHIK melt-quench simulation was followed by a GAP equilibration using different number of time steps. Like in the simulation for the small-scale structures, the structures were minimized after equilibration with the GAP and subsequently CHIK single-point and CHIK re-relaxed energies were evaluated. Before the equilibration we evaluated the GAP minimized energies.

	ΔE (meV/SiO$_2$)				
	single-point evaluation				re-relaxed
	before equilibration		after equilibration		
Quench rate (Ks^{-1})	GAP	CHIK	GAP	CHIK	CHIK
10^{13}	308	316	218	428	317
10^{12}	249	273	169	374	273
10^{11}	226	254	147	352	254
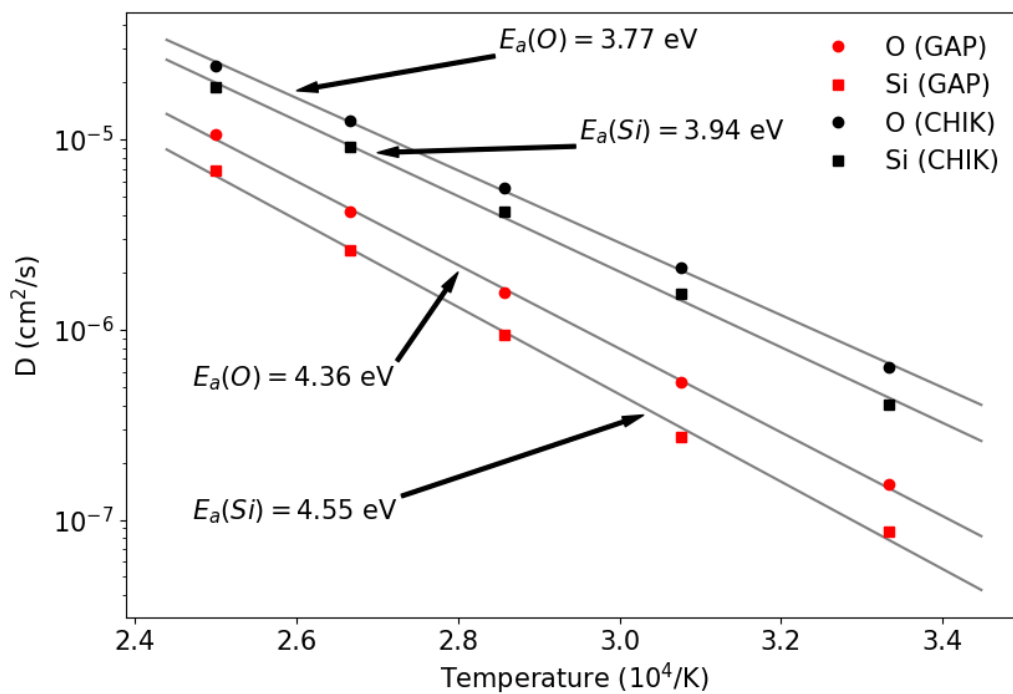
Supplementary Figure 4. Arrhenius plot for the self-diffusion constants of silicon and oxygen in liquid silica calculated using the GAP and CHIK potentials, respectively. The diffusion coefficients are determined using mean square displacements and the Einstein relation over a time scale of 200 ps. The used initial structure was the liquid structure (GAP) from Supplementary Figure 3, which was annealed to the target temperature in 40 ps and equilibrated for 10 ps. We wish to emphasise that the maximum mean square displacement for 3000 K and the GAP potential was only 1.5 Å^2 for silicon and 2.6 Å^2 for oxygen. Nevertheless, we determined a diffusion constants, since we clearly observed a linear trend.

* rohrer@mm.tu-darmstadt.de

† albe@mm.tu-darmstadt.de

‡ volker.deringer@chem.ox.ac.uk

[1] Larsen, A. H. *et al.* The atomic simulation environment—a Python library for working with atoms. *Journal of Physics: Condensed Matter* **29**, 273002 (2017).

[2] Mortensen, J. J., Hansen, L. B. & Jacobsen, K. W. Real-space grid implementation of the projector augmented wave method. *Physical Review B* **71**, 035109 (2005).

[3] Enkovaara, J. *et al.* Electronic structure calculations with GPAW: a real-space implementation of the projector augmented-wave method. *Journal of Physics: Condensed Matter* **22**, 253202 (2010).

[4] Kresse, G. & Hafner, J. Ab initio molecular dynamics for liquid metals. *Physical Review B* **47**, 558–561 (1993).

[5] Kresse, G. & Hafner, J. Ab initio molecular-dynamics simulation of the liquid-metal–amorphous-semiconductor transition in germanium. *Physical Review B* **49**, 14251–14269 (1994).

[6] Kresse, G. & Furthmüller, J. Efficiency of ab-initio total energy calculations for metals and semiconductors using a plane-wave basis set. *Computational Materials Science* **6**, 15–50 (1996).

[7] Kresse, G. & Furthmüller, J. Efficient iterative schemes for ab initio total-energy calculations using a plane-wave basis set. *Physical Review B* **54**, 11169–11186 (1996).

[8] Blöchl, P. E. Projector augmented-wave method. *Physical Review B* **50**, 17953–17979 (1994).

[9] Kresse, G. & Joubert, D. From ultrasoft pseudopotentials to the projector augmented-wave method. *Physical Review B* **59**, 1758–1775 (1999).

[10] Bloch, F. Bemerkung zur Elektronentheorie des Ferromagnetismus und der elektrischen Leitfähigkeit. *Zeitschrift für Physik* **57**, 545–555 (1929).

[11] Perdew, J. P. & Wang, Y. Accurate and simple analytic representation of the electron-gas correlation energy. *Physical Review B* **45**, 13244–13249 (1992).

[12] Perdew, J. P. & Zunger, A. Self-interaction correction to density-functional approximations for many-electron systems. *Physical Review B* **23**, 5048–5079 (1981).

[13] Perdew, J. P., Burke, K. & Ernzerhof, M. Generalized Gradient Approximation Made Simple. *Physical Review Letters* **77**, 3865–3868 (1996).

14 Perdew, J. P. *et al.* Restoring the Density-Gradient Expansion for Exchange in Solids and Surfaces. *Phys. Rev. Lett.* **100**, 136406 (2008).

15 Sun, J., Ruzsinszky, A. & Perdew, J. P. Strongly Constrained and Appropriately Normed Semilocal Density Functional. *Physical Review Letters* **115**, 036402 (2015).

16 Demuth, T., Jeanvoine, Y., Hafner, J. & Ángyán, J. G. Polymorphism in silica studied in the local density and generalized-gradient approximations. *Journal of Physics: Condensed Matter* **11**, 3833–3874 (1999).

17 Plimpton, S. Fast Parallel Algorithms for Short-Range Molecular Dynamics. *Journal of Computational Physics* **117**, 1–19 (1995).

18 Nosé, S. A molecular dynamics method for simulations in the canonical ensemble. *Molecular Physics* **52**, 255–268 (1984).

19 Hoover, W. G. Canonical dynamics: Equilibrium phase-space distributions. *Physical Review A* **31**, 1695–1697 (1985).

20 Parrinello, M. & Rahman, A. Polymorphic transitions in single crystals: A new molecular dynamics method. *Journal of Applied Physics* **52**, 7182–7190 (1981).

21 Belsky, A., Hellenbrandt, M., Karen, V. L. & Luksch, P. New developments in the Inorganic Crystal Structure Database (ICSD): accessibility in support of materials research and design. *Acta Crystallogr., Sect. B* **58**, 364–369 (2002).

22 Mazurin, O., Streltsina, M. & Shvaiko-Shvaikovskaya, T. *Silica Glass and Binary Silicate Glasses.* ISSN (2012).

23 Deringer, V. L. & Csányi, G. Machine Learning Based Interatomic Potential for Amorphous Carbon. *Phys. Rev. B* **95**, 094203 (2017).

24 Deringer, V. L. *et al.* Gaussian process regression for materials and molecules. *Chem. Rev.* **121**, 10073–10141 (2021).

25 Carré, A., Horbach, J., Ispas, S. & Kob, W. New fitting scheme to obtain effective potential from Car-Parrinello molecular-dynamics simulations: Application to silica. *EPL (Europhysics Letters)* **82**, 17001 (2008).

26 Akaogi, M. & Navrotsky, A. The quartz-coesite-stishovite transformations: new calorimetric measurements and calculation of phase diagrams. *Physics of the Earth and Planetary Interiors* **36**, 124–134 (1984).

27 Hemingway, B. S., Bohlen, S. R., Hankins, W. B., Westrum, E. F. & Kuskov, O. L. Heat capacity and thermodynamic properties for coesite and jadeite, reexamination of the quartz-coesite equilibrium boundary. *American Mineralogist* **83**, 409–418 (1998).

28 Akaogi, M., Yusa, H., Shiraishi, K. & Suzuki, T. Thermodynamic properties of α-quartz, coesite, and stishovite and equilibrium phase relations at high pressures and high temperatures. *Journal of Geophysical Research: Solid Earth* **100**, 22337–22347 (1995).

29 Bose, K. & Ganguly, J. Quartz-coesite transition revisited: Reversed experimental determination at 500–1200 °C and retrieved thermochemical properties. *American Mineralogist* **80**, 231–238 (1995).

30 Holm, J., Kleppa, O. & Westrum, E. F. Thermodynamics of polymorphic transformations in silica. Thermal properties from 5 to 1070° K and pressure-temperature stability fields for coesite and stishovite. *Geochimica et Cosmochimica Acta* **31**, 2289–2307 (1967).

31 Piccione, P. M. *et al.* Thermochemistry of Pure-Silica Zeolites. *The Journal of Physical Chemistry B* **104**, 10001–10011 (2000).

32 Robie, R. A., Hemingway, B. S. & Fisher, J. R. Thermodynamic properties of minerals and related substances at 298.15 K and 1 bar (105 pascals) pressure and at higher temperatures. Tech. Rep. 1452, U.S. Geological Survey ; For sale by the Supt. of Docs., U.S. G.P.O., (1978).

33 Richet, P., Bottinga, Y., Denielou, L., Petitet, J. P. & Tequi, C. Thermodynamic properties of quartz, cristobalite and amorphous SiO_2: drop calorimetry measurements between 1000 and 1800 K and a review from 0 to 2000 K. *Geochimica et Cosmochimica Acta* **46**, 2639–2658 (1982).

34 Petrovic, I., Heaney, P. & Navrotsky, A. Thermochemistry of the new silica polymorph moganite. *Physics and Chemistry of Minerals* **23** (1996).

35 Mei, Q., Benmore, C. J., Sen, S., Sharma, R. & Yarger, J. L. Intermediate range order in vitreous silica from a partial structure factor analysis. *Physical Review B* **78**, 144204 (2008).

36 Mei, Q., Benmore, C. J. & Weber, J. K. R. Structure of Liquid SiO_2: A Measurement by High-Energy X-Ray Diffraction. *Physical Review Letters* **98**, 057802 (2007).

37 Weidner, D. J. & Carleton, H. R. Elasticity of coesite. *Journal of Geophysical Research (1896-1977)* **82**, 1334–1346 (1977).

38 Weidner, D. J., Bass, J. D., Ringwood, A. E. & Sinclair, W. The single-crystal elastic moduli of stishovite. *Journal of Geophysical Research: Solid Earth* **87**, 4740–4746 (1982).

39 Bechmann, R. Elastic and Piezoelectric Constants of Alpha-Quartz. *Physical Review* **110**, 1060–1061 (1958).

40 Yeganeh-Haeri, A., Weidner, D. J. & Parise, J. B. Elasticity of α-Cristobalite: A Silicon Dioxide with a Negative Poisson's Ratio. *Science* **257**, 650–652 (1992).

41 Levien, L., Prewitt, C. T. & Weidner, D. J. Structure and elastic properties of quartz at pressure. *American Mineralogist* **65**, 920–930 (1980).

42 Kato, K. & Nukui, A. Die Kristallstruktur des monoklinen Tief-Tridymits. *Acta Crystallographica Section B Structural Crystallography and Crystal Chemistry* **32**, 2486–2491 (1976).

43 Miehe, G. & Graetsch, H. Crystal structure of moganite: a new structure type for silica. *European Journal of Mineralogy* **4**, 693–706 (1992).

44 Downs, R. T. & Palmer, D. C. The pressure behavior of α cristobalite. *American Mineralogist* **79**, 9–14 (1994).

45 Kirfel, A. & Will, G. Ending the "P21/a coesite" discussion. *Zeitschrift für Kristallographie - Crystalline Materials* **167**, 287–292 (1984).

46 Díaz-Cabañas, M.-J. & Barrett, P. A. Synthesis and structure of pure SiO2 chabazite: the SiO2 polymorph with the lowest framework density. *Chemical Communications* 1881–1882 (1998).

47 Keskar, N. R. & Chelikowsky, J. R. Structural properties of nine silica polymorphs. *Physical Review B* **46**, 1–13 (1992).

48 Bohlen, S. R. & Boettcher, A. L. The quartz ? coesite transformation: A precise determination and the effects of other components. *Journal of Geophysical Research: Solid Earth* **87**, 7073–7078 (1982).

49 Wehinger, B. *et al.* Lattice dynamics of-cristobalite and the boson peak in silica glass. *Journal of Physics: Condensed Matter* **27**, 305401 (2015).

50 Bosak, A. *et al.* Lattice dynamics of stishovite from powder inelastic x-ray scattering. *Geophysical Research Letters* **36** (2009).